Grain-Boundary Structural Relaxation in Sb_2Se_3 Thin-Film Photovoltaics

R.A. Lomas-Zapata,[1] K.P. McKenna,[2] Q.M. Ramasse,[3,4] R.E. Williams,[1] L.J. Phillips,[5]
K. Durose,[5] J.D. Major,[5] and B.G. Mendis[1,*]

[1] *Department of Physics, Durham University, South Road, Durham DH1 3LE, UK*
[2] *School of Physics, Engineering and Technology, University of York, Heslington, York YO10 5DD, UK*
[3] *SuperSTEM, SciTech Daresbury Campus, Daresbury WA4 4AD, UK*
[4] *School of Chemical and Process Engineering, University of Leeds, Leeds LS2 9JT, UK*
[5] *Department of Physics, Stephenson Institute for Renewable Energy, University of Liverpool, Liverpool L69 7ZF, UK*

(Received 23 November 2023; revised 23 December 2023; accepted 12 January 2024; published 8 February 2024)

Grain boundaries play an important role in the efficiency of thin-film photovoltaics, where the absorber layer is invariably polycrystalline. Density-functional-theory simulations have previously identified a "self-healing" mechanism in Sb_2Se_3 that passivates the grain boundaries. During "self-healing," extensive structural relaxation at the grain boundary removes the band-gap electronic defect states that give rise to high carrier recombination rates. In this work, lattice imaging in a transmission electron microscope is used to uncover evidence for the theoretically proposed structural relaxation in Sb_2Se_3. The strain measured along the [010] crystal direction is found to be dependent on the nature of the grain-boundary plane. For a (010) grain boundary, the strain and structural relaxation is minimal, since no covalent bonds are broken by termination of the grain. On the other hand, strains of up to approximately 4% extending approximately 2 nm into the grain interior are observed for a (041) grain boundary, where grain termination results in significant structural relaxation due to the ideal atomic coordination being disrupted. These results are consistent with theory and suggest that Sb_2Se_3 may have a high level of grain-boundary-defect tolerance.

DOI: 10.1103/PRXEnergy.3.013006

I. INTRODUCTION

Sb_2Se_3 and its sulfur-alloyed variant $Sb_2(S,Se)_3$ are promising absorber-layer materials for thin-film photovoltaics, having achieved efficiencies slightly above 10% through a variety of deposition methods [1,2]. Apart from the earth abundance and nontoxicity of the constituent elements, a unique feature of Sb_2Se_3 is its crystal structure, which consists of $[Sb_4Se_6]_n$ ribbons oriented along the [001] direction of the orthorhombic unit cell (*Pbnm* space group [3]). The ribbons are held together by weak van der Waals bonding. As first noted by Zhuo *et al.* [4], electrically benign grain boundaries that are free of dangling bonds are produced for grain-boundary planes that pass through the van der Waals gap between the ribbons. This condition is, however, quite restrictive and difficult to achieve in practice, with the preferred grain texture tending to be either (211) or (221) [5–9], which inevitably results in the ribbon covalent bonding being disrupted at the grain-boundary plane. Therefore, grain boundaries can still potentially reduce the efficiency of $Sb_2(S,Se)_3$ thin-film photovoltaics, although there are likely to be other contributing factors as well, such as highly anisotropic charge transport [10], a nonideal window, back contact layers, deep-level intrinsic point defects, etc. [11].

Recent density-functional-theory (DFT) simulations have, however, reported a dramatic "self-healing" mechanism in Sb_2Se_3 and Sb_2S_3 free surfaces [12,13]. In particular, short intra-ribbon and long inter-ribbon bonds are newly formed, such that the coordination number of the surface Sb and S(e) atoms are at least equal to the minimum value in the bulk [13]. Surface reconstructions are known to occur in a wide variety of materials, including metals, semiconductors, and oxides [14]. However, $Sb_2S(e)_3$ is unique because the band-gap electronic defect states are completely eliminated by the surface reconstruction for *all* surfaces [13]. This property is termed "self-healing." DFT simulations on a (041) symmetric tilt boundary indicate that self-healing applies to grain

---

[*] b.g.mendis@durham.ac.uk

boundaries as well [12]. Therefore, there is a theoretical possibility that all $Sb_2S(e)_3$ grain boundaries are electrically benign, irrespective of the orientation of the grain-boundary plane with respect to the ribbons. This would be a significant advantage, since grain boundaries can severely limit the efficiency in inorganic thin-film photovoltaics, especially CdTe [15–17].

Characterization techniques such as low-energy electron diffraction (LEED) and scanning tunneling microscopy (STM) have traditionally been used to analyze the crystallography of surfaces [18]. Since grain boundaries are buried interfaces, the detection of any structural relaxation poses a unique set of challenges (see below). In this work, we use lattice imaging in a transmission electron microscope (TEM) to find evidence for structural relaxation at Sb_2Se_3 grain boundaries in a real photovoltaic device structure. Structural relaxation is not detected when the grain-boundary plane passes through the van der Waals gap but is significant otherwise (i.e., approximately 4% maximum strain) and can extend a few nanometers into the grain interior. While the measurements do not directly provide electronic structure information, the experimental results are consistent with DFT predictions of $Sb_2S(e)_3$ undergoing large deformations to reduce its interfacial energy and point to grain-boundary behavior that is unique among inorganic photovoltaic materials.

II. EXPERIMENTAL AND SIMULATION METHODS

Grain boundaries in two close-space-sublimated Sb_2Se_3 devices were analyzed. One of the devices had a CdS window layer, while in the other device, the window layer was TiO_2. The fabrication and performance of these devices are reported in Ref. [9]. Significant interdiffusion occurs at the CdS-Sb_2Se_3 interface [12], although the grain boundary analyzed in this work is toward the Sb_2Se_3 back surface and can therefore be regarded as being a "pure" Sb_2Se_3 grain boundary. Cross-section TEM samples were prepared using a FEI Helios 600 focused-ion-beam (FIB) microscope, with the gallium ion-beam voltage progressively reduced to 5 kV to minimize surface damage [19]. The back surface of the Sb_2Se_3 absorber layer was carbon coated to minimize charge build-up in the FIB microscope. High-resolution electron microscopy (HREM) images of Sb_2Se_3 grain boundaries in the TiO_2-Sb_2Se_3 sample were acquired in a JEOL 2100F field-emission-gun TEM operating at 200 kV. The energy-dispersive X-ray (EDX) chemical composition across the grain boundaries was measured using an Oxford Instruments X-Max 65 T silicon drift detector, with the microscope operating in scanning TEM (STEM) mode. Grain-boundary imaging for the CdS-Sb_2Se_3 sample was performed using the Nion UltraSTEM 100 MC Hermes microscope at the SuperSTEM facility in Daresbury. This is an aberration-corrected STEM operating at 60 kV and 31-mrad probe semiconvergence angle. High-angle annular dark-field (HAADF) images of the grain boundary were acquired with 82-mrad inner and 180-mrad outer angle annular detector. To analyze the structural relaxation, the grain boundary must be tilted "end-on" and should ideally be straight, with very little projected width. Since images are acquired in projection, only the structural-relaxation component that is normal to the grain-boundary plane can be detected. Furthermore, HREM images in an uncorrected TEM show lattice fringes instead of "point" intensity maxima for most zone axes in Sb_2Se_3. Consequently, lattice fringes must ideally be parallel to the grain-boundary plane to simplify the interpretation of any structural relaxation. These conditions are difficult to satisfy simultaneously, so that multiple samples (>12) had to be prepared to find suitable grain boundaries.

Spin-polarized DFT calculations were carried out using the Vienna *ab initio* simulation package (VASP) [20,21]. Consistent with our previous work on extended defects in Sb_2Se_3 [12,13], we employed the HSE06 hybrid functional [22] and the D3 Grimme dispersion correction [23]. The bulk crystal was optimized using a 350-eV plane-wave cutoff and a $2 \times 2 \times 6$ Γ-centered k-point grid for Brillouin-zone sampling, leading to lattice constants corresponding to the *Pbnm* space group of $a = 11.520$ Å, $b = 11.912$ Å, and $c = 3.976$ Å. The (001) surface was described using a supercell containing a two-dimensionally periodic slab of 12 repeats of the bulk unit cell (approximately 46 Å thick) and an approximately 16 Å vacuum gap. The supercell was optimized (constant volume) with HSE06 + D3 until all forces were less than 0.01 eV/Å.

Supercells for modeling the (010)|(041) asymmetric grain boundary were constructed from the optimized bulk structures using the GBMaker code [24], with grain thicknesses of 20–30 Å. A small mismatch in lattice parameters parallel to the grain boundary is accommodated by applying a small ($<0.1\%$) strain shared equally between the grains in order to make them commensurate. Optimization is performed for different intergrain translation states (using a 5×4 grid) in order to identify stable grain-boundary structures. Due to the large size of the supercell, optimization (with respect to the position of all atoms and the length of the supercell perpendicular to the grain-boundary plane) is performed using the PBE + D3 functional and $2 \times 1 \times 1$ k-point grid. The stability of different models is compared by computing grain-boundary formation energies (E_f):

$$E_f = \frac{E_{GB} - \sum_i n_i \mu_i}{2A}, \tag{1}$$

where E_{GB} is the total energy of the grain-boundary supercell, A is the cross-section area of the grain boundary, n_i is the number of atoms of each species i in the supercell, and μ_i is the corresponding chemical potential. For stoichiometric supercells, the formation energy depends on the total (free) energy per formula unit of Sb_2Se_3. For nonstoichiometric supercells, the formation energy depends on the chemical potential of Sb or Se and is computed between Se-poor (defined by pure Sb) and Se-rich (defined by pure Se) limits. Following this procedure, two low-formation-energy grain-boundary structures are identified: a Se-rich structure with a formation energy ranging from 0.49 J/m^2 (Se-poor) to 0.37 J/m^2 (Se-rich) and a stoichiometric structure with a formation energy of 0.40 J/m^2. All supercell structures were visualized using the VESTA software package [25].

III. RESULTS AND DISCUSSION

Figure 1(a) is an aberration-corrected STEM HAADF image of a Sb_2Se_3 grain boundary located close to the back surface of the absorber layer. The amorphous

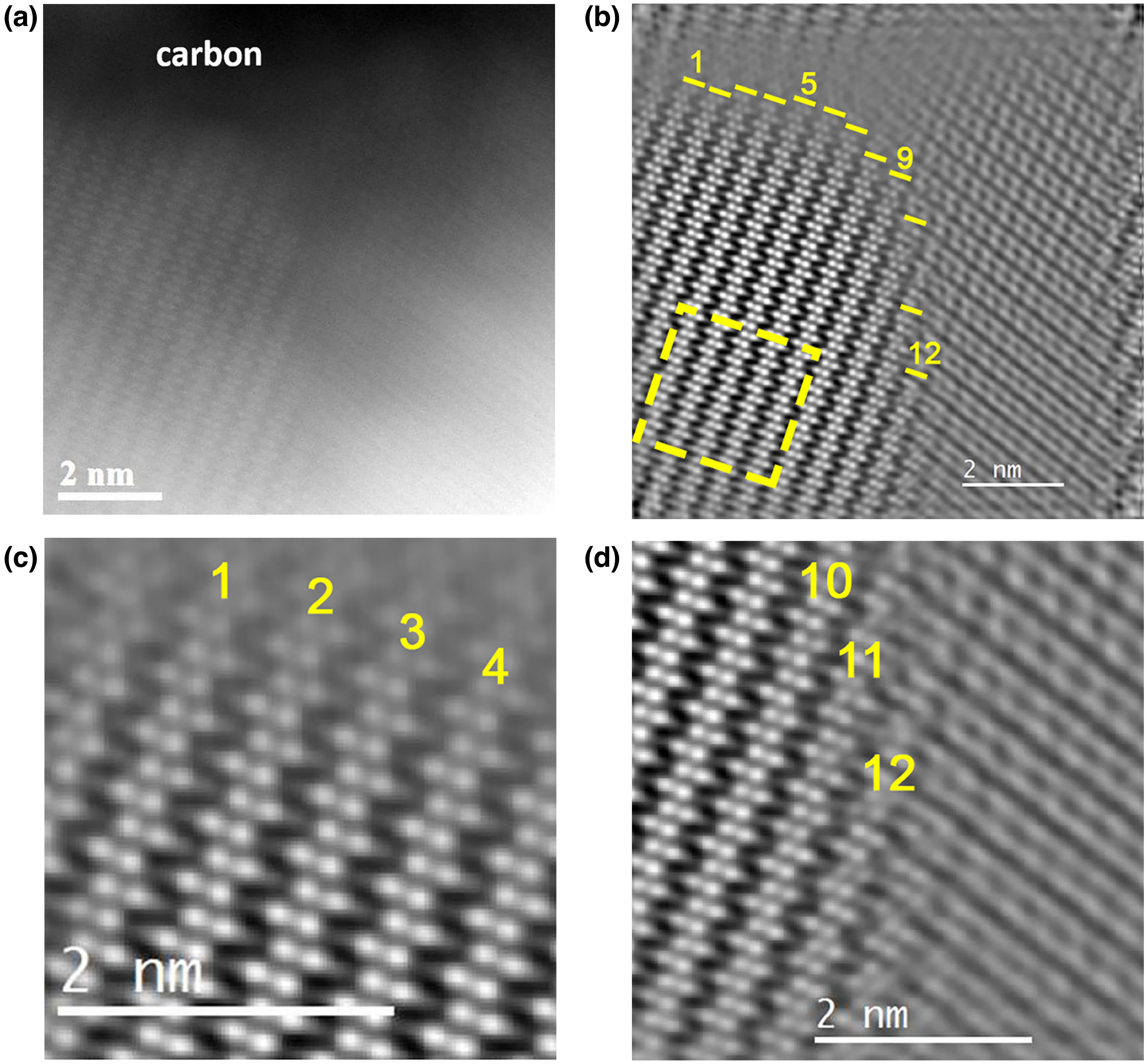

FIG. 1. (a) A raw HAADF image of a grain boundary close to the Sb_2Se_3 back surface. The carbon coating at the top is deposited during TEM-specimen preparation. The image is adapted from Ref. [12]. Reproduced with permission; copyright American Chemical Society. (b) The same HAADF image after Fourier filtering. Strain analysis is performed on 12 $[Sb_4Se_6]_n$ ribbons numbered in ascending order from left to right (for clarity, only a few of the numbers are shown). The approximate end positions of the ribbons are annotated, as well as the box region used to estimate the reference Sb-atom column pair spacing in the “bulk” crystal. (c),(d) Enlarged views of the regions where ribbons terminate at the Sb_2Se_3 back surface and grain boundary, respectively.

carbon layer at the top is deposited during TEM specimen preparation (Sec. II). The image was acquired from the CdS-Sb_2Se_3 device and has been previously reported in Ref. [12]. The left-hand grain is tilted to the [100] zone axis, while the right-hand grain is close to the $[2\bar{1}1]$ orientation. The grain-boundary plane is indexed as (041) in the crystal coordinates of the left-hand grain [12]. The Fourier-filtered image [Fig. 1(b)] shows the atomic structure of the $[Sb_4Se_6]_n$ ribbons more clearly in the left grain. Due to the strong atomic number contrast in HAADF images [26], only the heavy Sb atoms are visible, while the signal-to-noise ratio is not sufficient to observe the lighter Se atoms. The Sb-atom columns are paired on the (002) planes and show a zig-zag arrangement along the ribbon direction. Strain analysis of neighboring Sb column pairs along the [001] ribbon direction was performed on 12 $[Sb_4Se_6]_n$ ribbons, as labeled in Fig. 1(b). Ribbons 1–9 extend to the Sb_2Se_3 back surface (i.e., the interface between the Sb_2Se_3 layer and the carbon coating), while the other ribbons terminate at the grain-boundary plane. The HAADF intensity line profile across the full length of a given ribbon was extracted and a Gaussian function fitted to individual intensity maxima, in order to obtain more accurate Sb pair positions. The Sb pair spacing along [001] in the "bulk" region, away from the back surface and grain boundary, was also measured to provide a reference value for the undistorted crystal. The annotated box region in Fig. 1(b) was used for this purpose. Apart from the mean Sb pair spacing in the "bulk," the standard deviation and standard error were also calculated to quantify the measurement error.

The Sb pair spacing along the [001] direction as a function of the pair index is shown for each of the 12 ribbons in Fig. 2. The pair indices refer to the numbering scheme used to identify Sb column pairs on neighboring (002) planes. Smaller pair indices are located deeper within the Sb_2Se_3 grain interior and the minimum and maximum values for a given ribbon depend on its end positions in the HAADF image. The mean pair spacing in the "bulk" crystal and the measurement error (i.e., the standard deviation and the standard error) are also superimposed in each plot. Ribbons 1–9, which terminate at the back surface, do not show pair spacings significantly above the standard deviation apart from the Sb column pairs closest to the back surface. There is a loss of HAADF contrast close to the back surface [Fig. 1(c)], which has some curvature and is therefore not perfectly end-on. Hence Sb column pairs close to the back surface will be at different specimen depths, which lowers the HAADF contrast due to a nonoptimal image defocus [27]. It is believed that the larger variation in Sb pair spacing close to the back surface is an artifact of the lower contrast rather than a genuine feature of the specimen. This is even more apparent for ribbons 10–12, which terminate at the grain-boundary plane. Large variations in Sb pair spacings are observed over an appreciable distance from the grain boundary (Fig. 2). Apart from any grain-boundary curvature, there is also overlap with the weak crystalline contrast from the neighboring grain [Fig. 1(d)], which introduces further errors in the peak fitting (note that for ribbons 1–9 there is only a uniform background from the amorphous carbon layer, which is removed during Fourier filtering).

The experimental results for ribbons 1–9 can be compared with the DFT simulations for a (001) Sb_2Se_3 free surface. Supercells for an unrelaxed and relaxed (001) free surface are shown in Fig. 3(a). Significant displacement of the surface Sb atoms is observed due to formation of intra- and inter-ribbon bonds during relaxation. Using the unrelaxed crystal as a guide, it is possible to track the average position of the Sb-atom pairs in a single (002) plane; a few example (002) planes are labeled in Fig. 3(a). Sb-atom pair spacings along [001] in the relaxed supercell can therefore be determined and compared directly with experiment. A plot of the Sb-atom pair spacing versus the pair index for the DFT supercell is shown in Fig. 3(b). The graph has mirror symmetry due to periodic boundary conditions in DFT. The Sb pair spacing shows an oscillatory behavior, with large deviations from the perfect crystal value occurring close to the free surface. The strain at the free surface is 32% but decreases rapidly to a negligible value within only ten (002) planes away from the free surface, equivalent to approximately 2 nm. Since the strain is highly localized and oscillatory, its detection via HAADF imaging would require a perfectly flat free surface, which unfortunately is not the case for Fig. 1. Furthermore, the experimental Sb_2Se_3 back surface is in contact with an amorphous carbon layer, rather than vacuum, as assumed in DFT. The role of amorphous carbon on (001) surface relaxation is unknown but any changes to the structural relaxation must be confined to the near-surface region, since no significant strain was experimentally measured within the grain interiors (ribbons 1–9, Fig. 2). It could be argued that the two free surfaces of a thin TEM specimen could also alter the strain profile. Furthermore, despite careful control of the FIB TEM specimen preparation procedure (Sec. II), the free surfaces will invariably be modified by Ga implantation and ion-beam damage, potentially up to a depth of a few nanometers, although the exact value depends on the material and precise experimental conditions [28]. Electron-energy-loss-spectroscopy (EELS) measurements nevertheless indicate that the thicknesses of the TEM samples are approximately 45–60 nm (see the Supplemental Material [29]), which is sufficiently thick to display bulklike behavior. Furthermore, projected TEM or STEM images cannot detect the out-of-plane strain component, which is likely to be the most affected by the TEM foil-free surfaces.

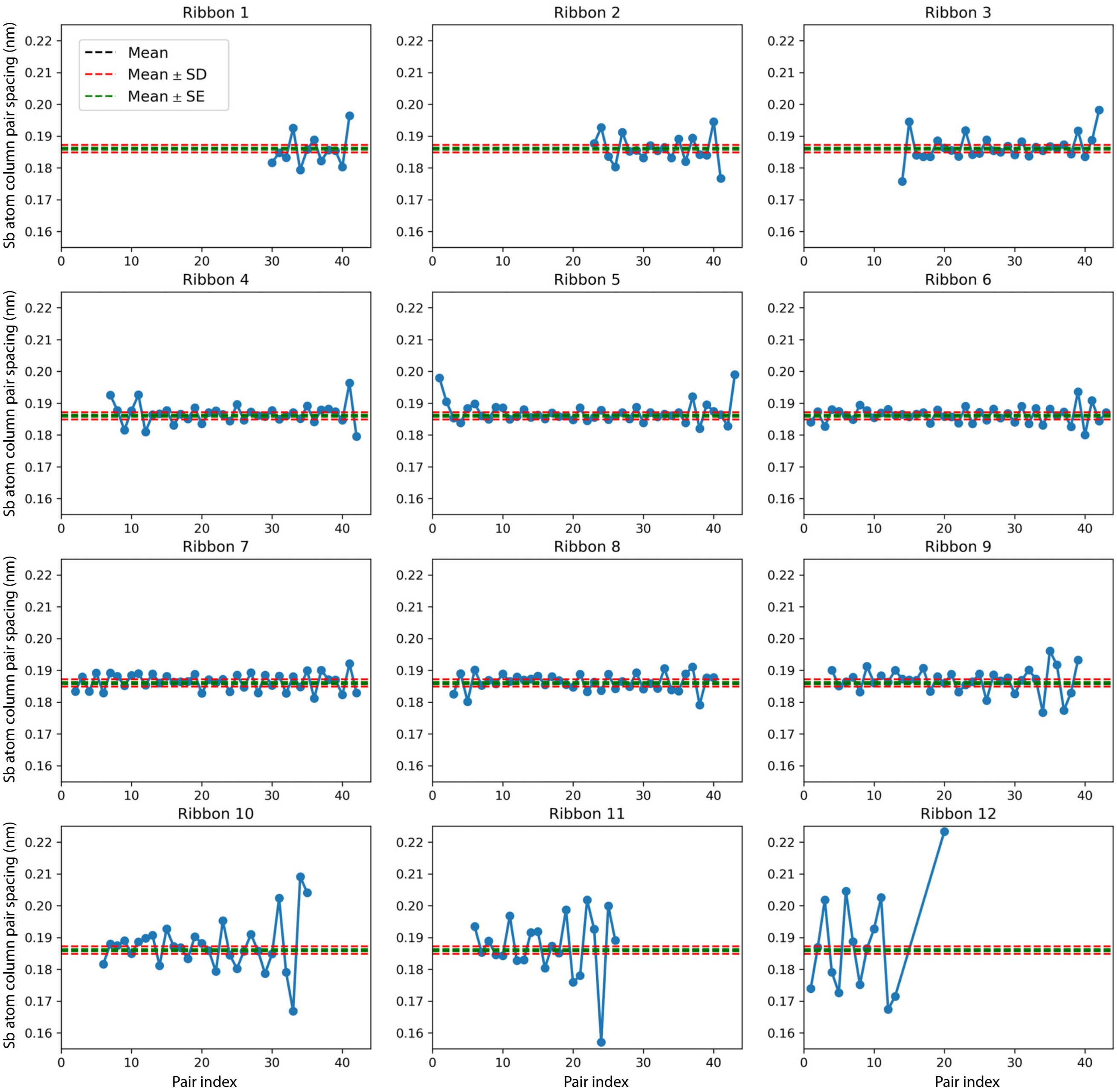

FIG. 2. The Sb-atom column pair spacing (y axis, expressed in nanometers) along [001] as a function of the pair index (x axis) for each of the 12 ribbons in Fig. 1(b). The pair indices increase in ascending order from the grain interior to the back surface–grain boundary. The range of pair indices for a given ribbon depends on the start and end positions for that ribbon in Fig. 1(b). The mean pair spacing for the "bulk" crystal, as well as the standard deviation and standard-error limits, are superimposed in each plot. The standard-error limits are close to the mean and therefore difficult to distinguish in the figure.

The HAADF image can also be used to measure any grain-boundary relaxation along the [010] direction. An intensity line scan across a given (002) crystal plane was used to measure the inter-ribbon distances along [010]; the ribbon position is defined as the average position of its two Sb atoms in the (002) plane. Four such line scans are shown in Fig. 4(a) and the corresponding results for inter-ribbon distances as a function of the ribbon pair index are plotted in Fig. 4(b). Larger ribbon pair indices are located closer to the grain boundary. The mean inter-ribbon distance for the "bulk," as well as the standard deviation and standard-error limits, are extracted from the yellow box in Fig. 1(b). In general, there is a systematic increase in the inter-ribbon distance toward the grain boundary. The increase is larger for line-scan rows 3 and 4, which are located further away from the Sb_2Se_3 back surface. It is therefore assumed that rows 3 and 4 are more indicative of true grain-boundary behavior. The systematic

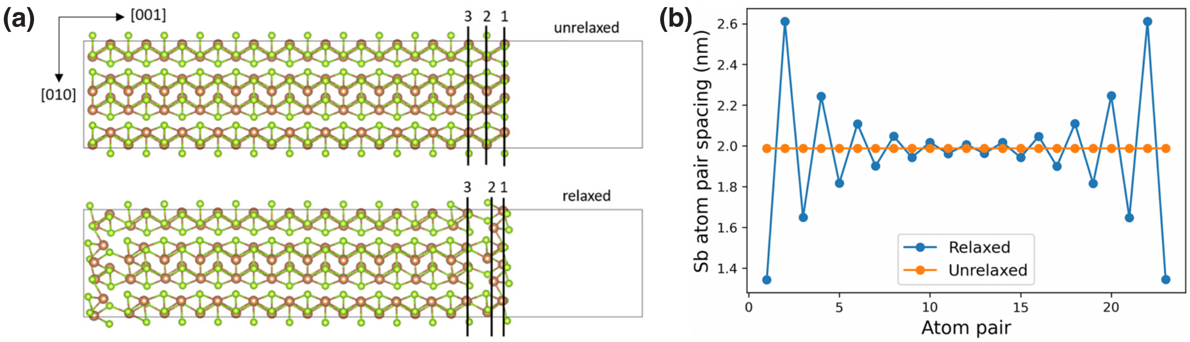

FIG. 3. (a) Unrelaxed and relaxed DFT supercells for a Sb_2Se_3 (001) free surface. Sb and Se atoms are displayed in brown and green shading, respectively. A few near-surface (002) planes have been labeled to highlight the structural relaxation. (b) The Sb-atom column pair spacing along [001] as a function of the pair index for the DFT relaxed supercell. The graph is symmetrical due to periodic boundary conditions and contains an identical free surface at both extremes. The horizontal line is the Sb pair spacing in the unrelaxed supercell.

increase in rows 3 and 4 takes place over approximately three inter-ribbon distances, i.e., approximately 2 nm along the [010] direction. The maximum strain is estimated to be approximately 4%. The lower atomic contrast at the grain boundary [Fig. 1(d)] could introduce some artifacts, such as the anomalous decrease in the last data point (i.e., ribbon pair index 12) for line-scan row 4. Nevertheless, the systematic increase in the inter-ribbon spacing over physical distances well away from the grain-boundary plane suggests that genuine structural relaxation is present, likely caused by the $[Sb_4Se_6]_n$ ribbons terminating at the grain-boundary plane. The resulting dangling bonds and electronic defect states are expected to be "healed" via structural relaxation in a manner similar to free surfaces. Previous DFT simulations have predicted self-healing in a (041) symmetric tilt boundary [12]; a similar calculation on the lower-symmetry grain boundary in Fig. 1 is, however, difficult to perform due to the large number of atoms in the supercell.

The structural relaxation along a given crystallographic direction (e.g., [010]) is highly dependent on the nature of the grain-boundary plane. To illustrate this, consider the HREM image of the Sb_2Se_3 grain boundary shown in Fig. 5(a), which was acquired from the TiO_2-Sb_2Se_3 device. The right-hand grain was tilted to the [100] major zone axis, which leaves the left-hand grain close to the $[10\bar{2}]$ orientation [fast Fourier transforms for the two grains are shown in Figs. 5(b) and 5(c), respectively]. (020) lattice fringes, which can be used to measure the strain along [010], are common to both grains. For the left grain, the (020) fringes are parallel to the grain-boundary plane, while in the right grain they intersect the grain boundary at an angle of 26°. The grain-boundary-plane Miller indices are therefore (010) and (061) in the crystal coordinates for the left- and right-hand grains, respectively. Unlike HAADF, strain analysis in HREM images is complicated by contrast reversals due to changes in specimen thickness and TEM foil bending [30]. To detect small changes in contrast, the HREM image was displayed on a color scale, as shown in Fig. 5(d). The left-hand grain has near-uniform contrast and is ideal for strain analysis. Strain analysis was also attempted on the right-hand grain, which showed

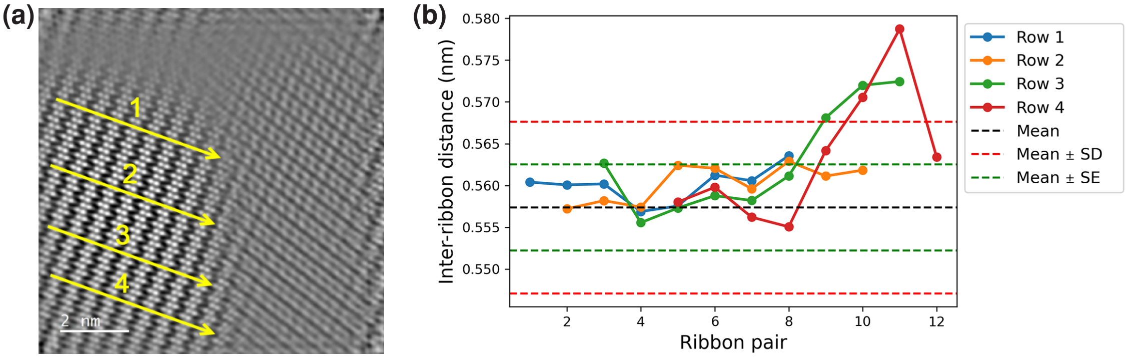

FIG. 4. (a) The same HAADF image as Fig. 1(b), showing the four line-scan rows used for calculating the inter-ribbon strain along [010]. (b) The [010] inter-ribbon distance as a function of the ribbon pair index for each of the rows in (a). The pair indices increase in ascending order from the grain interior to the grain boundary. The mean inter-ribbon distance for the "bulk" crystal, as well as the standard deviation and the standard-error limits, are also superimposed.

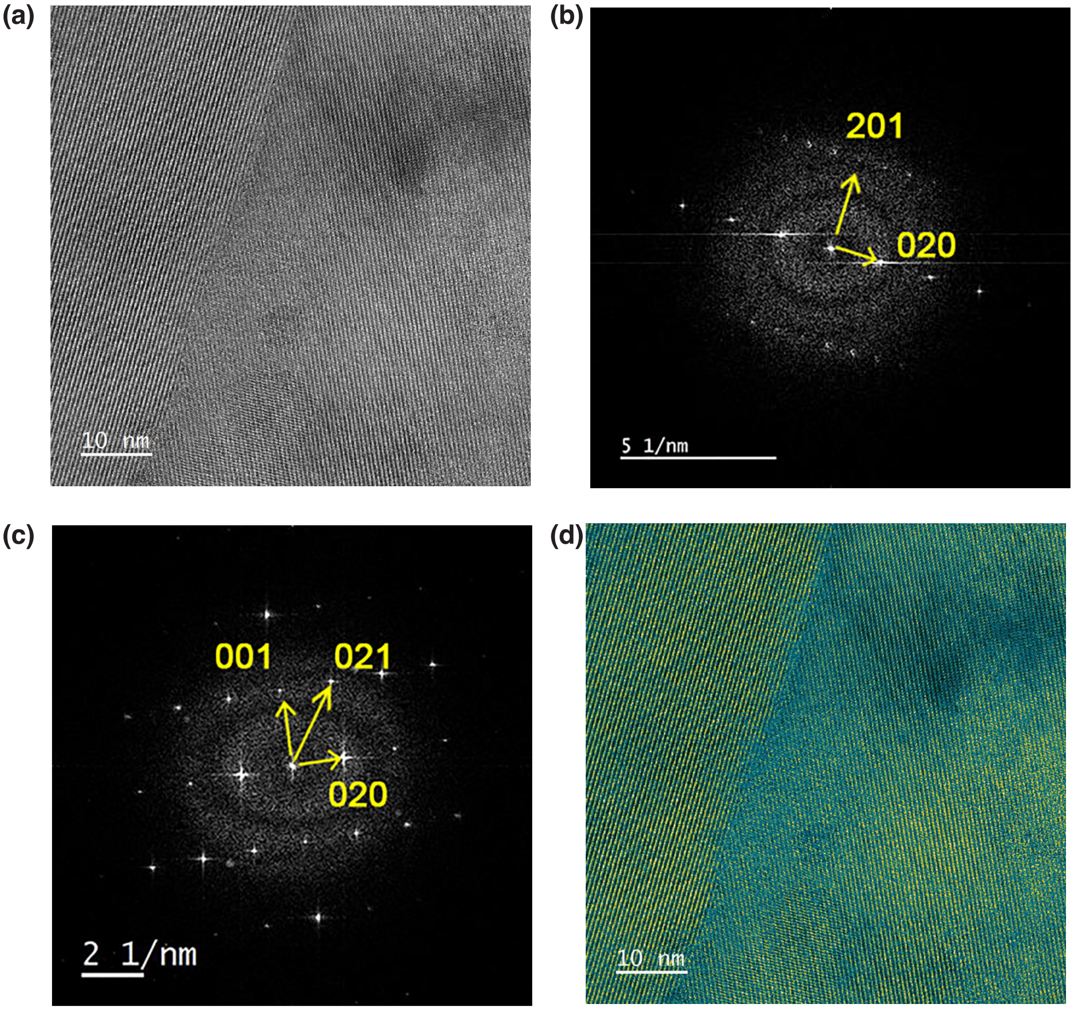

FIG. 5. (a) An HREM image of a Sb_2Se_3 grain boundary. The fast Fourier transforms for the left- and right-hand grains are shown in (b) and (c), respectively. (d) The same HREM image plotted on a color intensity scale to highlight subtle changes in the contrast.

nonuniform contrast, but the results were highly variable and no consistent trends were observed.

To quantify the [010]-direction strain in the left grain, the HREM image was first Fourier filtered, retaining only the (020) reflections for that grain [Fig. 6(a)]. Integrated line-intensity profiles along [010] were then extracted from selected box regions close to the grain boundary [see the annotated red boxes in Fig. 6(a)]. The (020) lattice fringe positions were determined by fitting Gaussian profiles to the intensity maxima. Multiple smaller box regions were chosen instead of a single large box, since the grain boundary is not perfectly straight and because it allows the reproducibility of any observed structural relaxation to be checked. A region away from the grain boundary was also chosen to measure the mean, standard deviation, and standard error of the (020) fringe spacing in the “bulk” [see the annotated yellow box in Fig. 6(a)]. Figure 6(b) shows the (020) lattice fringe spacing as a function of the fringe pair index for the three grain-boundary box regions in Fig. 6(a), labeled “top,” “center,” and “bottom,” respectively. Smaller fringe pair indices are located deeper within the grain interior and the estimated grain-boundary position is marked with a vertical dashed line in Fig. 6(b). For all regions analyzed, the (020) fringe spacings lie close to the mean value for the “bulk” and are well within the standard deviation of the measurement. This indicates an absence of [010] strain for the left-hand grain.

The (010) grain-boundary plane is parallel to the $[Sb_4Se_6]_n$ ribbons in the left-hand grain and can therefore occupy the van der Waals gap. Since no covalent bonds in the left grain are broken, any structural relaxation will be minimal. However, it is possible that there is structural relaxation with the neighboring right-hand grain, which has its $[Sb_4Se_6]_n$ ribbons terminating at the grain-boundary plane [Fig. 5(a)]. This is clear from the DFT results for the stoichiometric (010)|(041) asymmetric

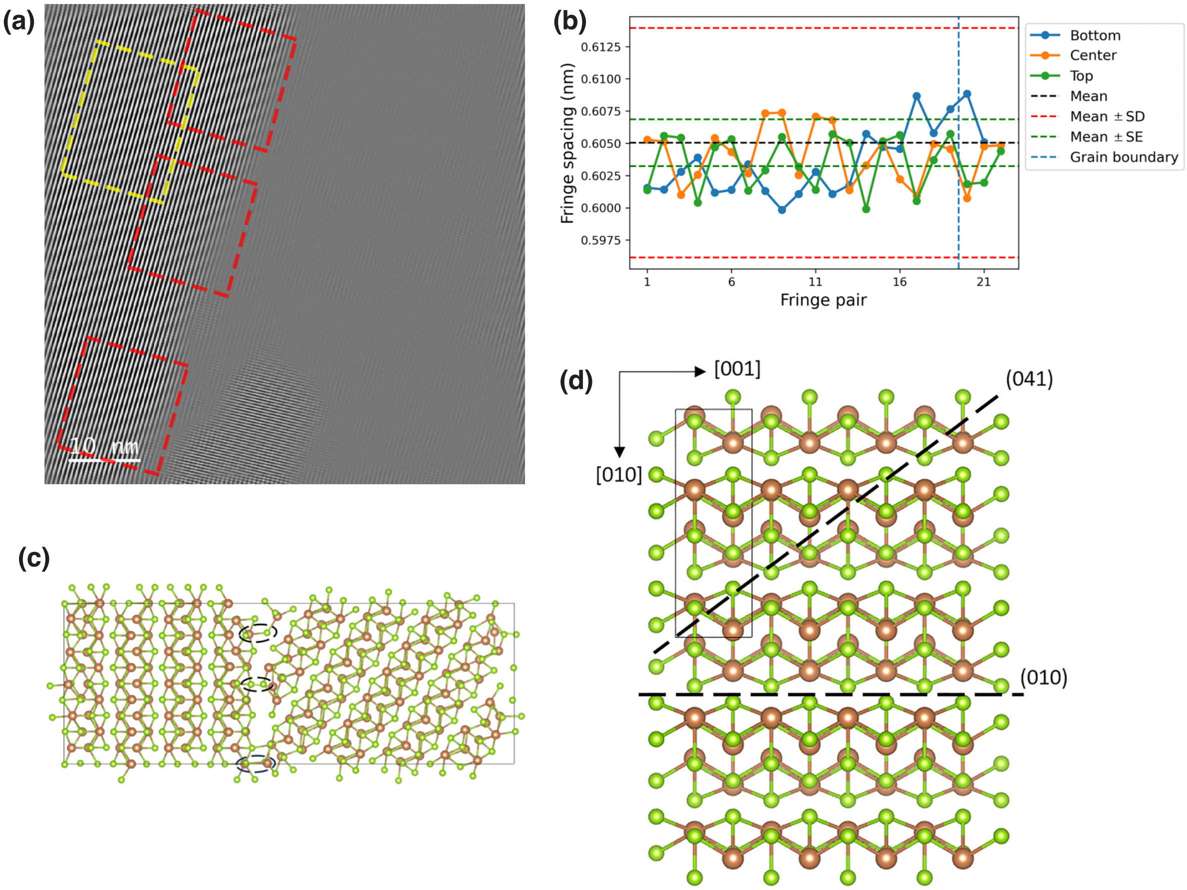

FIG. 6. (a) The Fourier-filtered image of Fig. 5(a), showing only the (020) lattice fringes in the left-hand grain. The red boxes indicate regions used for grain-boundary strain analysis, while the yellow box was used to analyze the “bulk” crystal. (b) The (020) lattice fringe spacing as a function of the fringe pair index for the “top,” “center,” and “bottom” grain-boundary box regions in (a). The pair indices increase in ascending order from the grain interior to the grain boundary. The vertical dashed line is the estimated position of the grain-boundary plane. The mean (020) fringe spacing for the bulk crystal, as well as the standard deviation and standard-error limits, are also superimposed. (c) The DFT supercell of a stoichiometric (010)|(041) asymmetric grain boundary, showing intergrain structural relaxation (a few intergrain bonds are circled). (d) Traces of the (041) and (010) planes in a Sb_2Se_3 crystal, viewed in projection along [100]. The box is an outline of a single unit cell. Sb and Se atoms are displayed in brown and green shading, respectively.

grain boundary in Fig. 6(c), where the $[Sb_4Se_6]_n$ ribbons for the left grain are parallel to the grain boundary but are misoriented at an angle of 37° in the right-hand grain. Despite no covalent bonds being broken in the left grain, there are new bonds being formed between the two sets of ribbons either side of the grain boundary. Intergrain bonds were also observed for the nonstoichiometric (i.e., Se-rich) (010)|(041) asymmetric grain boundary (see the Supplemental Material [29]). It was not possible to simulate the grain boundary in Fig. 5(a) due to the large number of atoms in the DFT supercell. However, it is likely that the intergrain structural relaxation observed for the simulated grain boundary [Fig. 6(c)] is also present in the experimental grain boundary [Fig. 5(a)]. From Fig. 6(c), the intergrain relaxation is largely confined to the ribbon closest to the grain-boundary plane and therefore not detected in the strain analysis [Fig. 6(b)] due to the limited sensitivity of the measurement and/or artifacts arising from any grain-boundary curvature.

The grain-boundary results can be summarized with the aid of Fig. 6(d). Here, the traces of the two grain-boundary planes analyzed, i.e., (041) and (010), are superimposed on the Sb_2Se_3 perfect crystal structure in [100] orientation. It is possible to select a (010) grain-boundary plane that lies entirely within the van der Waals gap. Since no covalent bonds are broken, this is presumed to be the lowest-energy configuration, and the structural relaxation is therefore minimal, consistent with the experimental results [Fig. 6(b)]. The (041) grain boundary will, however, always pass through some $[Sb_4Se_6]_n$ ribbons and therefore structural relaxation was experimentally observed, as expected [Fig. 4(b)]. We have also performed HREM strain analysis on (110) and (120) grain-boundary planes (see the Supplemental Material [29]). The HREM images show contrast reversals and are not ideal for strain analysis. Nevertheless, the results provide some evidence for strain relaxation, consistent with the breaking of $[Sb_4Se_6]_n$ ribbon covalent bonds at the grain boundary. Furthermore, EDX chemical analysis suggests that there may also be a change in stoichiometry at these grain boundaries. Nonstoichiometric grain boundaries have previously been reported in CdTe [31] and $Cu(In, Ga)Se_2$ [32] thin-film photovoltaics. Segregation of vacancy and antisite-atom point defects at the grain boundary will inevitably have some effect on the structural relaxation. Further work, possibly using aberration-corrected electron microscopy, is required to unambiguously confirm any nonstoichiometry at Sb_2Se_3 grain boundaries.

IV. SUMMARY AND CONCLUSIONS

HAADF and HREM imaging were used to test the structural relaxation theoretically predicted to occur at Sb_2Se_3 free surfaces and grain boundaries. Structural relaxation of $[Sb_4Se_6]_n$ ribbons at a (001) surface could not be detected due to curvature of the absorber-layer back surface. Relaxation along the [010] direction was also analyzed for (041) and (010) grain-boundary planes, respectively. Strain due to structural relaxation was observed for the former but not the latter. These observations are consistent with the (010) grain-boundary plane lying within the van der Waals gap, while the (041) grain-boundary plane will inevitably disrupt some of the $[Sb_4Se_6]_n$ ribbon covalent bonds. While the measurements confirm the presence of structural relaxation, they cannot provide any direct information on "self-healing," where electronic defect states within the band gap are eliminated in the relaxed grain boundary or free surface (scanning tunneling spectroscopy [18] could potentially be used to measure the electronic density of states, provided that a suitable specimen is used for such analysis). In particular, the structural relaxation is driven by total energy minimization, rather than a consideration of only the electronic energy levels. Nevertheless, it is reasonable to speculate that the two are often interrelated, in the sense that any structural relaxation is accompanied by removal of at least some of the deep electronic states. This has important implications for Sb_2Se_3 as a thin-film photovoltaic material. It suggests that polycrystalline Sb_2Se_3 is intrinsically tolerant to grain boundaries, unlike other materials such as CdTe, where the grain boundaries must be extrinsically passivated by chlorine doping. Finally, it should be pointed out that the structural relaxation in Sb_2Se_3 has an important role beyond free surfaces and grain boundaries. For example, recent DFT simulations have predicted negative-U vacancy defects [33] and bipolarons [34] that can impact the intrinsic doping and charge transport properties, respectively. In both cases, structural relaxation of the $Sb_2S(e)_3$ bonds is essential for stabilizing the defects or quasiparticles.

All data relating to the DFT calculations created during this research are available on request from the University of York Research database and at Ref. [35].

ACKNOWLEDGMENTS

R.A.L.-Z. would like to thank the Mexican government Consejo Nacional de Ciencia y Tecnología (CONACYT) scholarship program for Ph.D. funding. The instrument time at the Engineering and Physical Sciences Research Council (EPSRC) National Research Facility for Advanced Electron Microscopy, SuperSTEM, is also gratefully acknowledged (Grant EP/W021080/1). Via our membership of the United Kingdom HEC Materials Chemistry Consortium, which is funded by EPSRC (EP/R029431 and EP/X035859), this work used the ARCHER2 UK National Supercomputing Service and the Viking Cluster, which is a high-performance computer facility provided by the University of York. Funding for the work at Liverpool was provided by EPSRC via grant EP/W03445X/1.

[1] Y. Zhao, S. Wang, C. Jiang, C. Li, P. Xiao, R. Tang, J. Gong, G. Chen, T. Chen, J. Li, and X. Xiao, Regulating energy band alignment via alkaline metal fluoride assisted solution post-treatment enabling $Sb_2(S, Se)_3$ solar cells with 10.7% efficiency, Adv. Energy Mater. **12**, 2103015 (2022).

[2] Z. Duan, X. Liang, Y. Feng, H. Ma, B. Liang, Y. Wang, S. Luo, S. Wang, R. E. I. Schropp, Y. Mai, and Z. Li, Sb_2Se_3 thin-film solar cells exceeding 10% power conversion efficiency enabled by injection vapor deposition technology, Adv. Energy Mater. **34**, 2202969 (2022).

[3] T. D. C. Hobson and K. Durose, Protocols for the Miller indexing of Sb_2Se_3 and a non-x-ray method of orienting its single crystals, Mater. Sci. Semicond. Process. **127**, 105691 (2021).

[4] Y. Zhou, L. Wang, S. Chen, S. Qin, X. Liu, J. Chen, D.-J. Xue, M. Luo, Y. Cao, Y. Cheng, E. H. Sargent, and J. Tang, Thin-film Sb_2Se_3 photovoltaics with oriented one-dimensional ribbons and benign grain boundaries, Nat. Photonics **9**, 409 (2015).

[5] C. Chen, L. Wang, L. Gao, D. Nam, D. Li, K. Li, Y. Zhao, C. Ge, H. Cheong, H. Liu, H. Song, and J. Tang, 6.5% certified efficiency Sb_2Se_3 solar cells using PbS colloidal quantum dot film as hole-transporting layer, ACS Energy Lett. **2**, 2125 (2017).

[6] O. S. Hutter, L. J. Phillips, K. Durose, and J. D. Major, 6.6% efficient antimony selenide solar cells using grain structure control and an organic contact layer, Sol. Energy Mater. Sol. Cells **188**, 177 (2018).

[7] D.-B. Li, X. Yin, C. R. Grice, L. Guan, Z. Song, C. Wang, C. Chen, K. Li, A. J. Cimaroli, R. A. Awni, D. Zhao, H. Song, W. Tang, Y. Yan, and J. Tang, Stable and efficient CdS/Sb_2Se_3 solar cells prepared by scalable close space sublimation, Nano Energy **49**, 346 (2018).

[8] X. Wen, C. Chen, S. Lu, K. Li, R. Kondrotas, Y. Zhao, W. Chen, L. Gao, C. Wang, J. Zhang, G. Niu, and J. Tang,

Vapor transport deposition of antimony selenide thin film solar cells with 7.6% efficiency, Nat. Commun. **9**, 2179 (2018).

[9] L. J. Phillips, C. N. Savory, O. S. Hutter, P. J. Yates, H. Shiel, S. Mariotti, L. Bowen, M. Birkett, K. Durose, D. O. Scanlon, and J. D. Major, Current enhancement via a TiO_2 window layer for CSS Sb_2Se_3 solar cells: Performance limits and high V_{oc}, IEEE J. Photovoltaics **9**, 544 (2019).

[10] R. A. Lomas-Zapata, A. W. Prior, and B. G. Mendis, A simulation study of the role of anisotropic charge transport and grain boundary recombination in thin-film Sb_2Se_3 photovoltaics, Sol. Energy **264**, 112054 (2023).

[11] C. H. Don, T. P. Shalvey, and J. D. Major, What can Sb_2Se_3 solar cells learn from CdTe? PRX Energy **2**, 041001 (2023).

[12] R. E. Williams, Q. M. Ramasse, K. P. McKenna, L. J. Phillips, P. J. Yates, O. S. Hutter, K. Durose, J. D. Major, and B. G. Mendis, Evidence for self-healing benign grain boundaries and a highly defective Sb_2Se_3-CdS interfacial layer in Sb_2Se_3 thin-film photovoltaics, ACS Appl. Mater. Interfaces **12**, 21730 (2020).

[13] K. P. McKenna, Self-healing of broken bonds and deep gap states in Sb_2Se_3 and Sb_2S_3, Adv. Energy Mater. **7**, 2000908 (2021).

[14] P. R. Watson, Critical compilation of surface structures determined by low-energy electron diffraction crystallography, J. Phys. Chem. Ref. Data **16**, 953 (1987).

[15] J. D. Major, Grain boundaries in CdTe thin film solar cells: a review, Semicond. Sci. Technol. **31**, 093001 (2016).

[16] J. D. Major, Y. Y. Proskuryakov, K. Durose, G. Zoppi, and I. Forbes, Control of grain size in sublimation-grown CdTe, and the improvement in performance of devices with systematically increased grain size, Sol. Energy Mater. Sol. Cells **94**, 1107 (2010).

[17] B. G. Mendis, D. Gachet, J. D. Major, and K. Durose, Long lifetime hole traps at grain boundaries in CdTe thin-film photovoltaics, Phys. Rev. Lett. **115**, 218701 (2015).

[18] M. Prutton, *Introduction to Surface Physics* (Oxford University Press, Oxford, 1995).

[19] M. Schaffer, B. Schaffer, and Q. Ramasse, Sample preparation for atomic resolution STEM at low voltages by FIB, Ultramicroscopy **114**, 62 (2012).

[20] G. Kresse and J. Furthmüller, Efficiency of *ab-initio* total energy calculations for metals and semiconductors using a plane-wave basis set, Comput. Mater. Sci. **6**, 15 (1996).

[21] G. Kresse and J. Furthmüller, Efficient iterative schemes for *ab initio* total energy calculations using a plane-wave basis set, Phys. Rev. B **54**, 11169 (1996).

[22] A. V. Krukau, G. E. Scuseria, J. P. Perdew, and A. Savin, Hybrid functionals with local range separation, J. Chem. Phys. **129**, 124103 (2008).

[23] S. Grimme, Accurate description of van der Waals complexes by density functional theory including empirical constants, J. Comput. Chem. **25**, 1463 (2004).

[24] A. Kerrigan and K.P. McKenna, GBMaker v1.0.0 (Github, 2022) (https://doi.org/10.5281/zenodo.6334740).

[25] K. Momma and F. Izumi, VESTA 3 for three dimensional visualisation of crystal, volumetric and morphology data, J. Appl. Crystallogr. **44**, 1272 (2011).

[26] S. J. Pennycook and D. E. Jesson, High resolution *Z*-contrast imaging of crystals, Ultramicroscopy **37**, 14 (1991).

[27] D. O. Klenov and S. Stemmer, Contributions to the contrast in experimental high-angle annular dark-field images, Ultramicroscopy **106**, 889 (2006).

[28] J. Mayer, L. A. Giannuzzi, T. Kamino, and J. Michael, TEM sample preparation and FIB-induced damage, MRS Bull. **32**, 400 (2007).

[29] See the Supplemental Material at http://link.aps.org/supplemental/10.1103/PRXEnergy.3.013006 for (i) the TEM-specimen thickness, (ii) the intergrain bonding at the Se-rich (010)|(041) asymmetric grain boundary, (iii) the (110) grain-boundary strain and chemical composition, and (iv) the (120) grain-boundary strain and chemical composition.

[30] J. C. H. Spence, *High-Resolution Electron Microscopy*, 2nd ed. (Oxford University Press, Oxford, 2003).

[31] B. G. Mendis, Q. M. Ramasse, T. P. Shalvey, J. D. Major, and K. Durose, Optical properties and dielectric functions of grain boundaries and interfaces in CdTe thin-film solar cells, ACS Appl. Energy Mater. **2**, 1419 (2019).

[32] D. Abou-Ras, B. Schaffer, M. Schaffer, S. S. Schmidt, R. Caballero, and T. Unold, Direct insight into grain boundary reconstruction in polycrystalline $Cu(In, Ga)Se_2$ with atomic resolution, Phys. Rev. Lett. **108**, 075502 (2012).

[33] X. Wang, S. R. Kavanagh, D. O. Scanlon, and A. Walsh, Four electron negative-*U* vacancy defects in antimony selenide, Phys. Rev. B **108**, 134102 (2023).

[34] Y. Liu, B. Monserrat, and J. Wiktor, Strong electron-phonon coupling and bipolarons in Sb_2S_3, Phys. Rev. Mater. **7**, 085401 (2023).

[35] https://doi.org/10.15124/e53d5eaa-169b-48da-a3d1-34697c964f8c.